

Article

Catalytic Degradation of Toluene over $\text{MnO}_2/\text{LaMnO}_3$: Effect of Phase Type of MnO_2 on Activity

Lu Li ^{1,*}, Yuwei Liu ², Jingyin Liu ², Bing Zhou ², Mingming Guo ³ and Lizhong Liu ^{2,*}

¹ State Key Laboratory of Electrical Insulation and Power Equipment, Center of Nanomaterials for Renewable Energy, School of Electrical Engineering, Xi'an Jiaotong University, Xi'an 710049, China

² School of Chemistry and Chemical Engineering, Nantong University, 9, Seyuan Road, Nantong 226019, China

³ School of Environmental Science and Engineering, Shanghai Jiao Tong University, 800, Dong Chuan Road, Shanghai 200240, China

* Correspondence: dorislee1224@xjtu.edu.cn (L.L.); lzliu@ntu.edu.cn (L.L.)

Abstract: Series of α , β , γ , δ type MnO_2 supported on LaMnO_3 perovskite was developed by a one-pot synthesis route. Compared with α - MnO_2 , β - MnO_2 , γ - MnO_2 , δ - MnO_2 and LaMnO_3 oxides, all $\text{MnO}_2/\text{LaMnO}_3$ showed promotional catalytic performance for toluene degradation. Among them, α - $\text{MnO}_2/\text{LaMnO}_3$ holds the best active and mineralization efficiency. By the analysis of N_2 adsorption-desorption, XPS and H_2 -TPR, it can be inferred that the improved activity should be ascribed to the higher proportion of lattice oxygen, better low-temperature reducibility and larger specific surface area. Besides, the byproducts from the low-temperature reaction of toluene oxidation were detected by a TD/GC-MS, confirming the presence of the intermediates. Combined with the in-situ DRIFTS, the catalytic degradation path of toluene oxidation has also been discussed in depth.

Keywords: phase type; perovskite; toluene; catalytic oxidation; degradation path



Citation: Li, L.; Liu, Y.; Liu, J.; Zhou, B.; Guo, M.; Liu, L. Catalytic Degradation of Toluene over $\text{MnO}_2/\text{LaMnO}_3$: Effect of Phase Type of MnO_2 on Activity. *Catalysts* **2022**, *12*, 1666. <https://doi.org/10.3390/catal12121666>

Academic Editors: Fan Lin and Jong-Ki Jeon

Received: 13 November 2022

Accepted: 13 December 2022

Published: 18 December 2022

Publisher's Note: MDPI stays neutral with regard to jurisdictional claims in published maps and institutional affiliations.



Copyright: © 2022 by the authors. Licensee MDPI, Basel, Switzerland. This article is an open access article distributed under the terms and conditions of the Creative Commons Attribution (CC BY) license (<https://creativecommons.org/licenses/by/4.0/>).

1. Introduction

Volatile organic compounds (VOCs) are harmful pollutants released into the environment resulting from a variety of commercial, industrial, and domestic practices [1–3]. Among them, toluene is a ubiquitous aromatic VOC and an important contributor to the formation of ozone (O_3) as well as a secondary organic aerosol (SOA) [2,4]. Meanwhile, toluene is easily absorbed by the skin and mucous membranes, which has devastating effects on human organs and metabolic systems [5]. Many traditional technologies, such as condensation, membrane separation, absorption, thermal incineration, and catalytic oxidation, have been utilized to control VOCs [6–8], wherein catalytic oxidation has been believed to be one of the most effective strategies, which could completely convert pollutants into harmfulness final products, carbon dioxide and water [9]. Catalysts are the key factor in catalytic oxidation technology. Generally, noble metal and non-precious metal catalysts are the two major types of materials applied in toluene catalytic combustion. However, noble metals, such as gold, palladium, platinum, ruthenium, etc., are easily restricted by their high cost, sintering, and poisoning in industrial applications [10]. On the contrary, non-noble mixed metal oxides have been considered universal candidates due to their wide source, low price, relatively high activity, and good anti-toxicity [11,12].

Metal oxides/perovskites (MO_x/ABO_3) are a typical class of non-noble mixed metal oxide compounds, especially Mn-based $\text{MnO}_2/\text{AMnO}_3$, which have been widely used in the fields of denitration, desulfurization and VOCs oxidation [13–15]. Si et al. synthesized a γ - $\text{MnO}_2/\text{LaMnO}_3$ catalyst by selectively removing surficial La cation from LaMnO_3 and obtained a superior catalytic performance on toluene oxidation [16]. Yang et al. studied the LaMnO_3 perovskite assembled by δ - MnO_2 through a gunpowder-like combustion method and pointed out that the boosted active phase-carrier interplays, improved redox

abilities led to good performance for toluene oxidation [17]. We also synthesized a γ - $\text{MnO}_2/\text{SmMnO}_3$ material by in-situ acid etching of SmMnO_3 and found that the composite of γ - MnO_2 was successfully exposed on the surface of SmMnO_3 , which improved the physicochemical properties, thus promoted toluene oxidation capacity [18]. Kim et al. [19] paid attention to different manganese valent oxides Mn_3O_4 , Mn_2O_3 , and MnO_2 in the catalytic combustion of benzene and toluene. Figueredo et al. [20] also made a comparison of different manganese oxides Mn_3O_4 , Mn_2O_3 , and their biphasic compound $\text{Mn}_3\text{O}_4/\text{Mn}_2\text{O}_3$ material on the catalytic evaluation of ethene and propene. However, little attention is paid to digging out the effect of different phase types of manganese dioxide supported on perovskites, as well as the degree of activating lattice oxygen and catalytic activity. Meanwhile, a simple modulation process of MnO_2 on the perovskite surface is also particularly important due to the practical point of view. Besides, the catalytic mechanism of catalysts and the degradation path of toluene still require great efforts to clarify.

Based on the above challenges, herein we provide a relatively simple synthesis route for $\text{MnO}_2/\text{LaMnO}_3$ preparation, in which the phase type (α , β , δ , and γ) of MnO_2 can be directly adjusted by controlling the proportion of manganese source precursors. Meanwhile, the activation degree of lattice oxygen on the surface could also be controlled by adjusting the surficial phase type of MnO_2 of LaMnO_3 . Combined with the characterizations of XRD, SEM, N_2 physisorption, XPS, H_2 -TPR, etc., the influence of the phases of MnO_2 in LaMnO_3 on the physical and chemical properties and the catalytic activities for toluene degradation were explored, as well as the internal relationship of structure and catalytic behavior was also in-depth discussion. Finally, the types of byproducts by the low-temperature catalytic oxidation of toluene and the degradation path of toluene oxidation were discussed.

2. Results and Discussion

2.1. Morphology and Crystal Phase Structure

The crystal structures of samples were characterized by XRD. As shown in Figure S1, the diffraction peaks at $2\theta = 22.94^\circ$, 32.78° , 38.47° , 40.16° , 40.64° , 46.84° , 52.62° , 52.96° , 58.10° , 58.70° , 68.02° , 68.70° and 78.10° , corresponding to the (012), (110), (113), (202), (006), (024), (122), (116), (214), (018), (220), (208), and (128) planes of LaMnO_3 (PDF# 50-0298) [21]. Meanwhile, as illustrated in Figure 1, it was found that the new peaks of α -MO/LMO (Figure 1a) at $2\theta = 28.84^\circ$ (310) and 37.5° (211), β -MO/LMO (Figure 1b) at $2\theta = 28.68^\circ$ (110), 37.32° (101), and 42.8° (111), γ -MO/LMO (Figure 1c) at $2\theta = 22.4^\circ$ (120), 34.5° (031), 37.14° (131), and 57.4° (160), and δ -MO/LMO (Figure 1d) at $2\theta = 12.68^\circ$ (001), and 25.2° (002), corresponded to the standard cards of PDF# 44-0141 (α - MnO_2) [22], PDF# 24-0735 (β - MnO_2) [23], PDF# 80-1098 (δ - MnO_2) [24], and PDF# 14-0644 (γ - MnO_2) [18], respectively, showing that the different phases types (α , β , δ , and γ) MnO_2 were successfully combined with LaMnO_3 perovskite. In addition, the full width at half maximum (FWHM) of the characteristic peaks at $2\theta = 32.78^\circ$ are 0.38° for LMO, 0.37° for α -MO/LMO, 0.31° for β -MO/LMO, 0.29° for δ -MO/LMO and 0.28° for γ -MO/LMO. Obviously, the FWHM at $2\theta = 32.78^\circ$ of α -MO/LMO is closer to that of LMO, indicating that the composite degree of α - MnO_2 on the surface of LaMnO_3 is better, which is beneficial to inhibit the further agglomeration of LaMnO_3 during the hydrothermal reaction.

Figure 2a–j shows the SEM images of LMO, α -MO/LMO, β -MO/LMO, δ -MO/LMO and γ -MO/LMO. As can be seen in Figure 2a,b, the morphology of the LMO sample exhibits a bulk structure with large pore sizes, indicating that the high-temperature preparation process caused the agglomeration of the LMO catalyst. When the α - MnO_2 was combined with LaMnO_3 , the composite showed an obvious porous structure (Figure 2c), and the surface of the LaMnO_3 framework was covered with a furry substance (Figure 2d), which should be the α - MnO_2 with stacking-nanoneedle structure [23]. These changes may imply an increase in the specific surface area of the catalyst, which is conducive to the contact between toluene molecules and the catalyst, promoting the catalytic oxidation of toluene. In addition, it can be observed from the SEM images of β -MO/LMO in Figure 2e,f that the morphology of β -MO/LMO is disorganized and a small amount of sheet-like structures

are mixed in the sample, indicating that the presence of β - MnO_2 in the composite [23,25]. Similarly, the large-scale flower-like structures are also found in Figure 2g,h, confirming the formation of δ - MnO_2 in the δ -MO/LMO sample [26,27]. However, when γ - MnO_2 and LaMnO_3 were combined, lots of ca. 50 nm nano-spherical particles and large-sized agglomerates appeared in the SEM image (Figure 2i,j). Combined with the analysis of XRD, it can be inferred that the nano-spherical particles should belong to γ - MnO_2 .

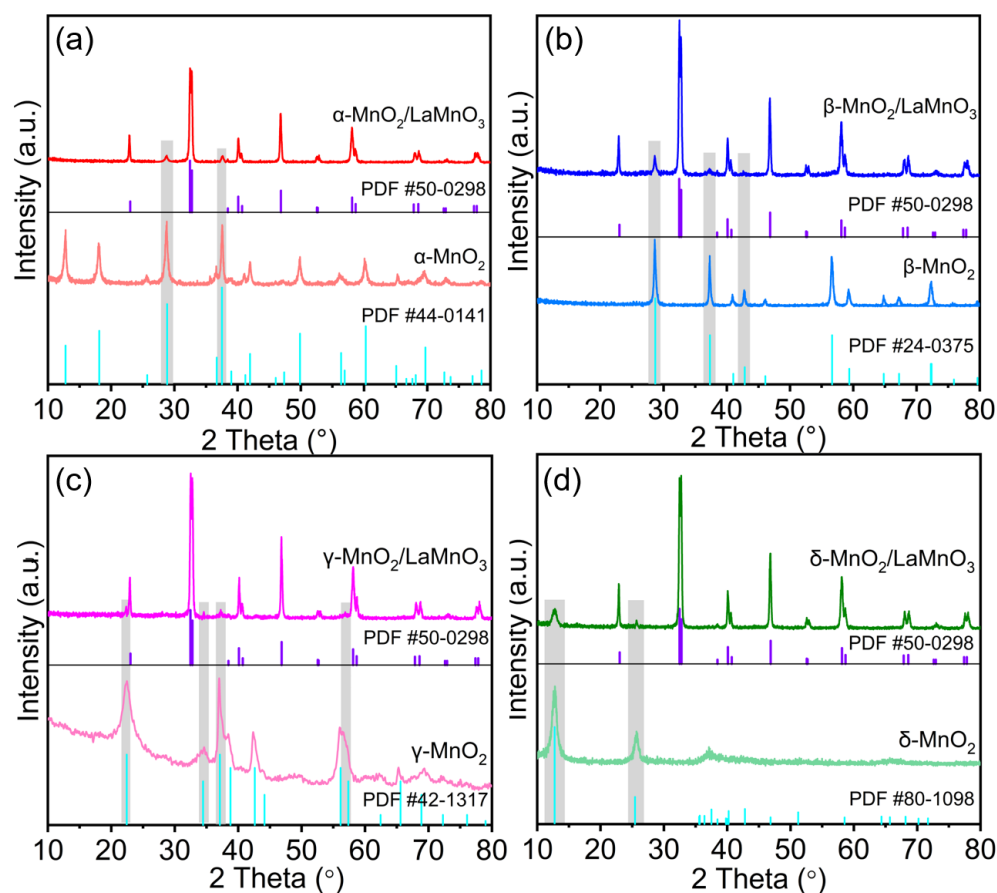


Figure 1. XRD patterns of (a) α -MO/LMO, α - MnO_2 and corresponding standard PDF card diffraction profile; (b) β -MO/LMO, β - MnO_2 and corresponding standard PDF card diffraction profile; (c) γ -MO/LMO γ - MnO_2 and corresponding standard PDF card diffraction profile; and (d) δ -MO/LMO, δ - MnO_2 and corresponding standard PDF card diffraction profile.

2.2. Catalytic Performance

Figure 3a demonstrates the toluene oxidation over LMO, α -MO/LMO, β -MO/LMO, δ -MO/LMO, and γ -MO/LMO. Before testing the properties of all samples, the blank experiment was performed without a catalyst, and the conversion was not found ($<320^\circ\text{C}$), indicating that there was no occurrence of homogeneous reactions under the adopted reaction [18,28]. The catalytic activities of all samples hoisted with the reaction temperature and the heightened sequence were as follows: $\text{LMO} < \gamma\text{-MO/LMO} < \delta\text{-MO/LMO} < \beta\text{-MO/LMO} < \alpha\text{-MO/LMO}$. Obviously, after loading manganese dioxide, the performance of new catalysts improved. Moreover, it can be seen from Figure S2 that the activity of each composite was also higher than that of the corresponding pure MnO_2 . In order to further analyze the catalytic activities of all catalysts, the T_{90} , and T_{50} values (reaction temperature vs. conversion of 50%, and 90%) were used to further assess their performance. As listed in Table 1, the T_{90} , and T_{50} values were 260 , and 237°C for α -MO/LMO, 289 , and 246°C for β -MO/LMO, 294 , and 255°C for δ -MO/LMO, 316 , and 261°C for γ -MO/LMO, >320 , and 300°C for LMO, 295 , and 252°C for α - MnO_2 , >320 , and 302°C for β - MnO_2 , >320 , and

289 °C for δ -MO, and > 320, and 286 °C for γ -MO, respectively. Obviously, α -MO/LMO holds lower T_{90} , and T_{50} values, indicating a better performance for toluene oxidation.

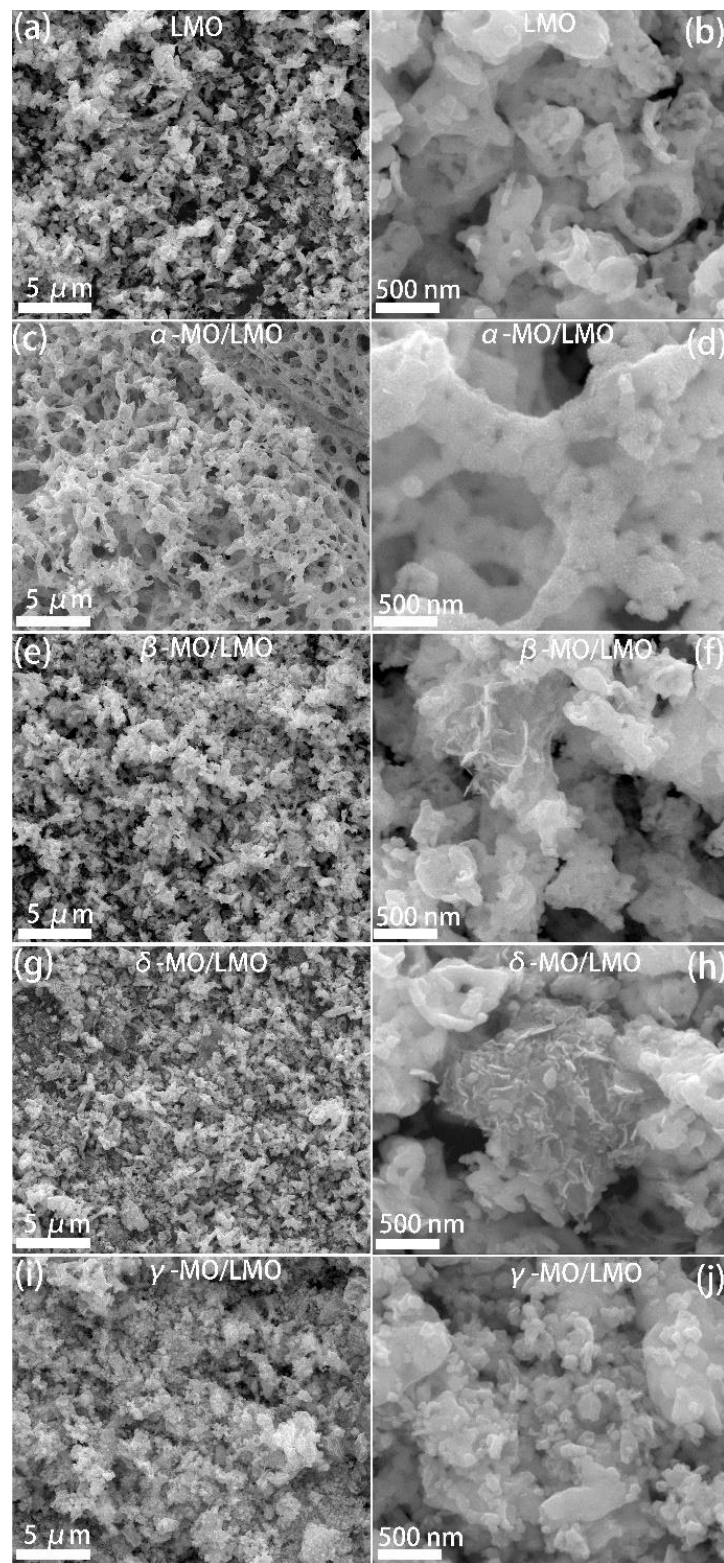


Figure 2. SEM images of (a,b) LMO, (c,d) α -MO/LMO, (e,f) β -MO/LMO, (g,h) δ -MO/LMO, and (i,j) γ -MO/LMO.

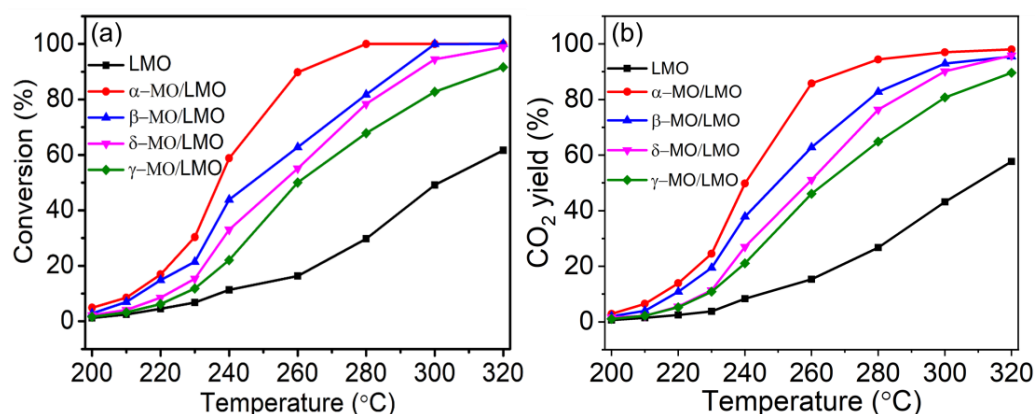


Figure 3. (a) Toluene conversion vs. temperature and (b) CO₂ yield over LMO, α -MO/LMO, β -MO/LMO, δ -MO/LMO, and γ -MO/LMO.

Table 1. Catalytic performance for toluene oxidation over various catalysts.

Samples	Conversion		CO ₂ Yield		<i>r</i> (10 ⁻¹⁰ mol m ⁻² s ⁻¹)
	<i>T</i> ₉₀ (°C)	<i>T</i> ₅₀ (°C)	<i>T</i> ₉₀ (°C)	<i>T</i> ₅₀ (°C)	
α -MO/LMO	260	237	269	241	3.13
β -MO/LMO	289	246	293	250	2.70
δ -MO/LMO	294	255	299	259	1.85
γ -MO/LMO	316	261	320	264	1.73
LMO	>320	300	>320	309	2.62
α -MO	295	252	/	/	/
β -MO	>320	302	/	/	/
δ -MO	>320	289	/	/	/
γ -MO	>320	286	/	/	/

Since the specific surface areas (S_{BET}) are quite different (shown in Table 2) and thermal effect may also exist at higher DCE conversion, the apparent reaction rates of these catalysts are calculated at low temperatures (210 °C) to reflect their inherent catalytic activities. As listed in Table 1, the values decrease in the sequence of α -MO/LMO > β -MO/LMO > LMO > δ -MO/LMO > γ -MO/LMO, which is basically consistent with the order for conversion efficiency, while LMO showed a higher apparent reaction rate than that of δ - and γ -phased samples.

Table 2. Surface element compositions, surface area and reducibility of LMO, α -MO/LMO, β -MO/LMO, δ -MO/LMO and γ -MO/LMO.

Catalysts	$S_{\text{BET}}/$ m ² ·g ⁻¹	Molar Ratios of Surface Elements by XPS		H ₂ uptake/mmol·g ⁻¹ (50–450 °C)
		Mn ⁴⁺ /Mn ³⁺	<i>O</i> _{latt} / <i>O</i> _{ads}	
LMO	14.0	0.38	1.21	2.03
α -MO/LMO	42.3	0.52	2.48	4.09
β -MO/LMO	40.0	0.46	2.39	3.51
δ -MO/LMO	39.6	0.42	2.12	3.03
γ -MO/LMO	35.6	0.40	1.89	2.44

To better evaluate the destruction ability of prepared catalysts, the mineralization efficiency of toluene oxidation was also measured. As shown in Figure 3b and Table 1, the mineralization temperatures of these catalysts for toluene are higher than that of conversion, where the variation trend of CO₂ yield was similar to that of conversion. Besides, α -MO/LMO sample still maintains the best behavior in CO₂ generation capacity.

2.3. Textual Structure and Surface Area

The N₂ adsorption-desorption isotherms of LMO, α -MO/LMO, β -MO/LMO, δ -MO/LMO and γ -MO/LMO are shown in Figure 4a, and the specific surface areas are listed in Table 2. As displayed in Figure 4a, the isotherms of LMO, α -MO/LMO, β -MO/LMO, δ -MO/LMO and γ -MO/LMO presented a typical IUPAC type II pattern with non-uniform slit pores (H3 type) of the hysteresis loop, signifying the existence of macroporous and mesoporous structures [11,18,29]. In addition, it can also be observed from the data listed in Table 2 that the specific surface areas of LMO, α -MO/LMO, β -MO/LMO, δ -MO/LMO, and γ -MO/LMO were 14.0, 42.3, 40.0, 39.6, and 35.6 m²·g⁻¹, respectively. Compared with pure perovskite, the specific surface areas of various phase types of MnO₂/LaMnO₃ were all increased. The high specific surface area is beneficial to promote the oxidation of toluene molecules on the surface of the catalyst [29,30]. Namely, the α -MO/LMO catalyst with the highest specific surface area may result in better activity [31].

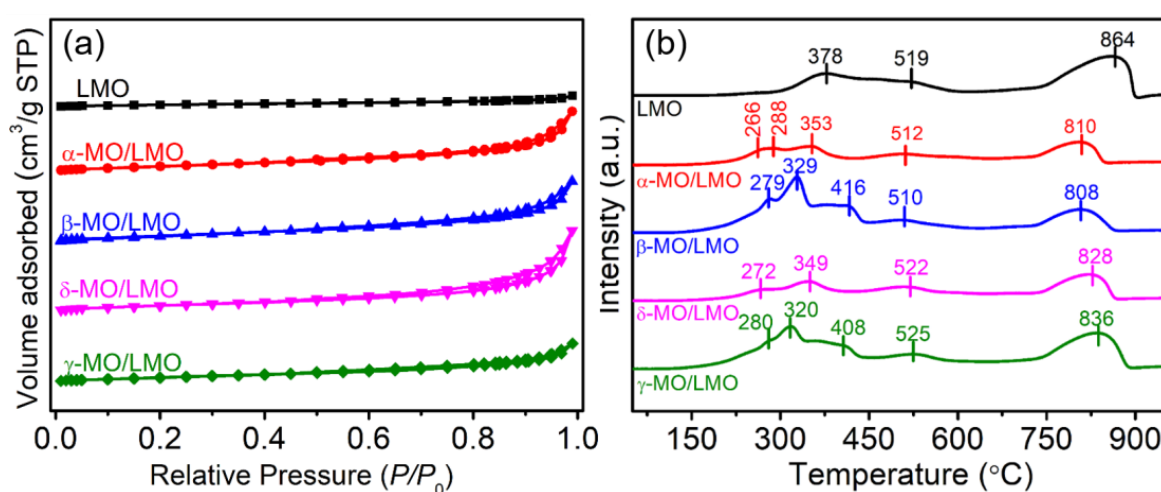


Figure 4. (a) N₂ adsorption-desorption isotherms and (b) H₂-TPR profiles of LMO, α -MO/LMO, β -MO/LMO, δ -MO/LMO and γ -MO/LMO.

2.4. Mn Oxidized State and Oxygen Species

The Mn-oxidized state and oxygen species on the surface of LMO, α -MO/LMO, β -MO/LMO, δ -MO/LMO, and γ -MO/LMO were obtained using XPS. The Mn 2p_{3/2}, O 1s XPS spectra of all catalysts are shown in Figure 5a,b and the quantitative analysis is presented in Table 2. As displayed in Figure 5a, the components divided from the Mn 2p_{3/2} XPS spectra at 643.58, 641.78, and 640.46 eV corresponded to Mn⁴⁺, Mn³⁺, and Mn²⁺, respectively [11,32–34]. Compared with that of pure LMO perovskite, the Mn 2p binding energy of MO/LMO is relatively reduced, suggesting that the density of the extranuclear electron cloud of the Mn element is increased. In fact, the asymmetric charge density distribution of Mn showed a significant increase in the hybridization of Mn 3d and O 2p orbitals and shortening of Mn–O bond length [21], which may be helpful to activate the lattice oxygen and improve the reducibility of the catalysts [12]. The increase in the molar ratio of Mn⁴⁺/Mn³⁺ in the order of LMO (0.38) < γ -MO/LMO (0.40) < δ -MO/LMO (0.42) < β -MO/LMO (0.46) < α -MO/LMO (0.52), which is consistent with the order of their activities. The increase in the proportion of high-valent manganese implies the lattice oxygen on the surface is more easily activated. The activated lattice oxygen can migrate to the oxygen vacancies and then transform into overflowed adsorbed oxygen species easily to oxidize toluene [21]. Consequently, the α -MO/LMO with the high molar ratio of Mn⁴⁺/Mn³⁺ has a higher toluene oxidation potential.

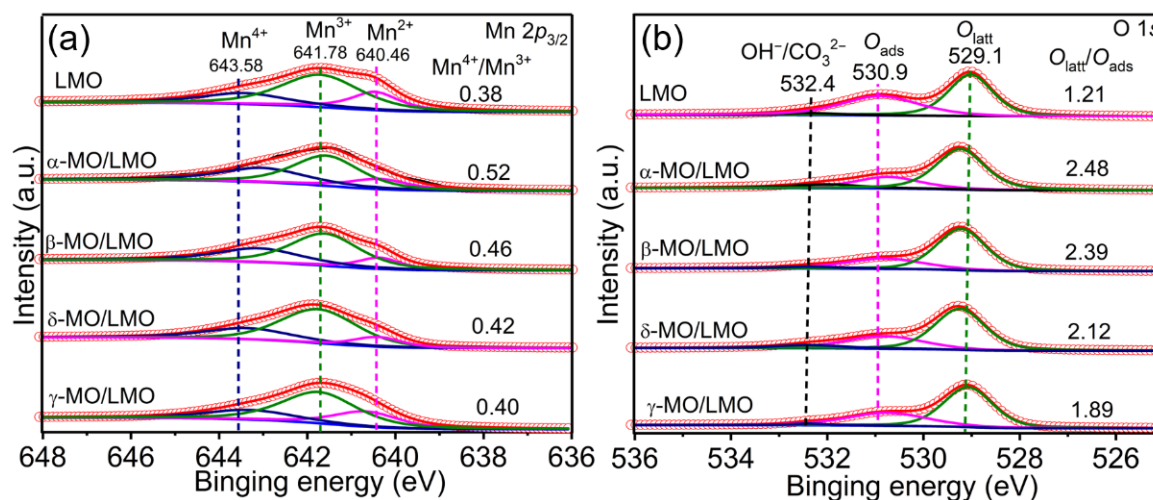


Figure 5. (a) Mn 2p_{3/2}, and (b) O 1s XPS spectra of LMO, α -MO/LMO, β -MO/LMO, δ -MO/LMO and γ -MO/LMO.

Furthermore, the oxygen species on the surface of all catalysts were determined by XPS. As shown in Figure 5b, the peaks of O 1s XPS spectra located at 529.1, 530.9, and 532.4 eV are attributed to the lattice oxygen (O_{latt}), surface adsorbed oxygen (O_{ads}) and surface carbonate (CO₃²⁻) or hydroxide (OH⁻), respectively [18,23,28]. In contrast to that of Mn 2p, the O 1s binding energy of MO/LMO is relatively elevated, explaining that the density of the extranuclear electron cloud of O element cut down, facilitating the activation of lattice oxygen. As listed in Table 2, the order of the O_{latt}/O_{ads} molar ratio enhanced in the arrangement of LMO (1.21) < γ -MO/LMO (1.89) < δ -MO/LMO (2.12) < β -MO/LMO (2.39) < α -MO/LMO (2.48), which is consistent with the increasing sequences of Mn⁴⁺/Mn³⁺ ratio and toluene conversion. The results testified that the composite of MnO₂ and LaMnO₃ promoted the enhancement of the activated lattice oxygen, and the surface of α -MO/LMO possessed the most O_{latt}, which induced the best catalytic oxidation performance of toluene.

2.5. Reducibility

The reducibility of LMO, α -MO/LMO, β -MO/LMO, δ -MO/LMO, and γ -MO/LMO was evaluated by H₂-TPR. As shown in Figure 4b, the peaks for LMO at 378 °C are attributed to the restituting of Mn⁴⁺, and the peak at 512 °C was assigned to the single-electron reduction of Mn³⁺ located in a coordination-unsaturated microenvironment, and the peak at 864 °C is classified to the retrieval of the left Mn³⁺ [18,24,26]. For α -MO/LMO, the peaks at 266 and 288 °C should correspond to the reduction of surface Mn⁴⁺ and deep Mn⁴⁺; the peaks at 353 and 512 °C belong to the reduction of surface Mn³⁺ and deep Mn³⁺; the peaks at 810 °C is pertain to the lowering of the left Mn³⁺ in LMO. Analogously, the peaks of β -MO/LMO at 279 and 329 °C belong to the surface Mn⁴⁺ and deep Mn⁴⁺, 416 and 510 °C corresponding to the reduction of surface Mn³⁺ and deep Mn³⁺, 808 °C corresponding to the left Mn³⁺ in LMO; the peaks of δ -MO/LMO at 272 °C corresponding to the reduction of Mn⁴⁺, 349 and 522 °C corresponding to the reduction of surface Mn³⁺ and deep Mn³⁺, 828 °C corresponding to the left Mn³⁺ in LMO; the peaks of γ -MO/LMO at 280 and 320 °C belong to the surface Mn⁴⁺ and deep Mn⁴⁺, 408 and 525 °C corresponding to the reduction of surface Mn³⁺ and deep Mn³⁺, 836 °C corresponding to the left Mn³⁺ in LMO. Obviously, α -MO/LMO has better reducibility at low temperatures. The H₂ consumption of each catalyst was calculated, and it can be confirmed from Table 2 that the order of hydrogen consumption between 50 and 450 °C is as follows: LMO (2.03 mmol·g⁻¹) < γ -MO/LMO (2.44 mmol·g⁻¹) < δ -MO/LMO (3.03 mmol·g⁻¹) < β -MO/LMO (3.51 mmol·g⁻¹) < α -MO/LMO (4.09 mmol·g⁻¹). Namely, the α -MO/LMO hold the high H₂-uptake, and the more H₂-uptake represents a higher valence of Mn [22,26], which indirectly shows that α -MO/LMO has more activated lattice oxygen on the surface, leading to the better toluene

oxidation. Combined with the results of H₂-TPR, XPS, BET and their activities, α -MO/LMO has a higher proportion of lattice oxygen, better low-temperature reducibility and larger surface area in comparison with other catalysts, which leads to the best catalytic activity.

2.6. Possible Degradation Mechanism

The rare content of exhaust byproducts was identified by the thermal desorption/gas chromatograph mass spectrometer instrument. As shown in Figure 6, trace byproducts from the T_{50} condition of α -MO/LMO oxidizing toluene illustrated some identifiable organic byproducts, such as benzene, benzoic acid, benzaldehyde, 1,3-diethenyl-benzene, acetic acid, benzyl alcohol, phenol, 4-phenyl-3-buten-2-one, octanoic acid, cyclohexasiloxane, tridecane, nonanoic acid, n-decanoic acid, benzophenone, and benzyl benzoate. In fact, toluene oxidation involves the surface active oxygen species excited by the heating [5,31,35]. Furthermore, the intermediates for the catalytic oxidation of toluene over α -MO/LMO were obtained and displayed in Figure 7. A series of structural changes in the surface of α -MO/LMO occurred. With the temperature change, the peak at 3070 cm⁻¹ belongs to the C-H of vinyl stretching vibration [36]. The peaks at 1596, 1533 and 1419 cm⁻¹ pertained to the C-C and C=O stretching vibration and carbonate species [37,38]. Moreover, the vibration modes at 1288 cm⁻¹ and 1038 cm⁻¹ belong to $\nu_s(\text{COO})$ stretching vibration [39]. The results showed that toluene was oxidized to some carbonyl-containing species. Even though a higher degradation efficiency was found for α -MO/LMO catalysts and only trace organic byproducts were detectable in the outgas, some of the products would cause more toxicity to human health or the environment [40], even in a very small quantity. The comprehensive assessment of these trace byproducts would be our future research direction to help the choice of new-dedicated catalysts for the VOC oxidation technique.

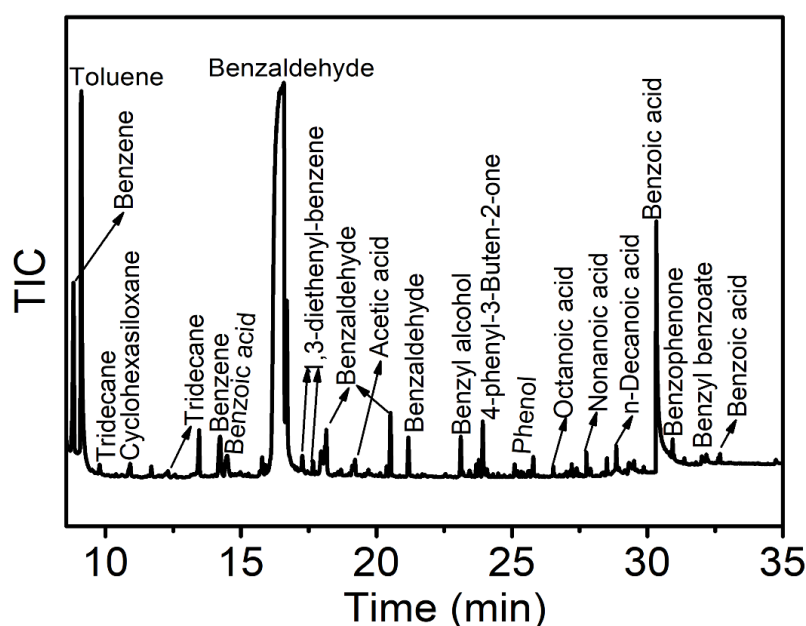


Figure 6. GC-MS spectrum of toluene oxidation over α -MO/LMO.

Based on the characterization of GC-MS and in-situ DRIFTS, the toluene oxidation over α -MO/LMO should adhere to the Mars-van Krevelen mechanism [41,42]. The active oxygen species on the surface of α -MO/LMO include adsorbed oxygen (O_{ads}) and lattice oxygen (O_{latt}). At a temperature, the activated O_{ads} and O_{latt} can be transformed into each other. Meantime, the consumed active oxygen can be repaired by the interaction of O_2 molecules in the atmosphere with oxygen vacancies. On account of a relatively low temperature, the number of excited reactive oxygen species on the surface of α -MO/LMO was limited, resulting in insufficient toluene oxidation, which can bring about a series of organic byproducts [18,21,43]. The toluene was decomposed and may undergo a series

of consequent reactions [18,24]: toluene \rightarrow benzyl alcohol \rightarrow benzaldehyde \rightarrow benzoic acid \rightarrow benzene \rightarrow acetic acid \rightarrow CO₂. Wherefore, it is necessary for toluene oxidation to further heighten the reaction temperature to manufacture more active oxygen species.

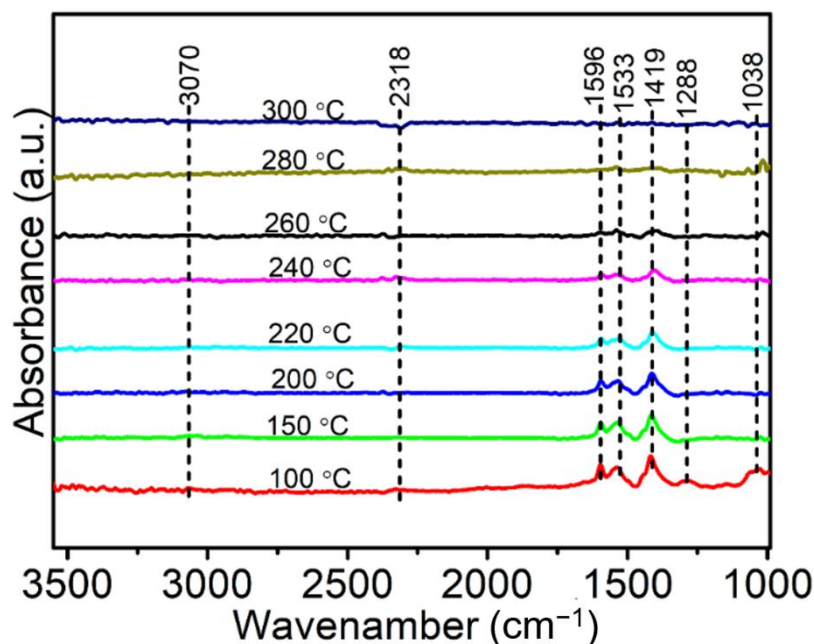


Figure 7. In-situ DRIFTS result of toluene oxidation over α -MO/LMO.

3. Experimental Section

3.1. Synthesis of Catalysts

LaMnO₃ perovskite was first prepared via direct calcination without adding water as solvent of metal salts and citric acid, which was similar to the preparation we previously reported [44]. α -MnO₂/LaMnO₃, β -MnO₂/LaMnO₃, δ -MnO₂/LaMnO₃, γ -MnO₂/LaMnO₃ (recorded as α -MO/LMO, β -MO/LMO, δ -MO/LMO, γ -MO/LMO) were synthesized by a simple one-step method, with the same molar ratio of MnO₂ to LaMnO₃ is 3:7. The typical synthesis procedure of α -MO/LMO was as follows: 0.35 g of KMnO₄ and 0.15 g of MnSO₄·H₂O was dissolved in 60 mL deionized water. After forming an emulsion-like, 2 g of LaMnO₃ powders were added to the above-mixed liquid and stirred for 30 min, and then transferred to a 100 mL PTFE kettle for hydrothermal reaction at 160 °C for 12 h. Ultimately, the acquired precipitates were calcined at 400 °C for 4 h.

For β -MO/LMO, 0.528 g of MnSO₄·H₂O and 0.712 g of (NH₄)₂S₂O₈ were added to 60 mL of deionized water. Other steps are similar to that of α -MO/LMO. For δ -MO/LMO, the addition amounts of KMnO₄ and MnSO₄·H₂O were 0.42 g and 0.78 g, respectively, and other steps were similar to that of α -MO/LMO. For γ -MO/LMO, 2 g of LaMnO₃, 0.3169 g of MnSO₄·H₂O, and 1 mL of concentrated H₂SO₄ were added to 60 mL deionized water and agitated at 80 °C for 30 min, then added 0.948 g of KMnO₄ to keep stirring for 24 h. The acquired precipitate was calcined at 400 °C for 4 h.

3.2. Characterization

The prepared samples were characterized by various measurement techniques, X-ray diffraction (XRD, Shimadzu, Tokyo, Japan), Scanning electron microscope (SEM, Bruker, Berlin, Germany), X-ray photoelectron spectra (XPS, Perkin-Elmer, Waltham, MA, USA), and H₂ temperature-programmed reduction (H₂-TPR, Micromeritics, Norcross, GA, USA). All the character processes and instrument parameters are detailed in the Supplementary Material document.

3.3. Catalytic Evaluation

The catalytic oxidation of toluene over all samples was estimated in a successive flow fixed bed quartz micro-reactor (I.D. = 0.006 m). 0.20 g of samples (80–120 mesh) were applied to investigate their properties. The air stream with approximately 1000 ppm of toluene crossed over the bed with a total flow rate of 40 mL/min, with a weight hourly space velocity (WHSV) of 12,000 mL/(g h⁻¹). The inlet and outlet concentration of toluene was detected by the GC with a flame ionization detector (FID).

The conversion of toluene is calculated by the following equations:

$$X = \frac{C_{\text{in}} - C_{\text{out}}}{C_{\text{in}}} \times 100\% \quad (1)$$

where X is the conversion efficiency of toluene, and C_{in} and C_{out} are the toluene concentrations in the inlet and outlet gas streams, respectively.

Meantime, the yield of CO₂, is resulted from Equation (2):

$$Y = \frac{C_{\text{CO}_2}}{6C_{\text{in}}} \times 100\% \quad (2)$$

where Y is the yield of CO₂, C_{CO_2} is the outlet CO₂ concentration.

For reaction products, the concentration of CO₂ from the outlet stream was measured on the GC-FID equipped with a nickel converting unit. Trace organic byproducts were trapped in a Carbopack B tube (Camsco, Huston, TX, USA) and then detected on a Gas Chromatograph Mass Spectrometer (Agilent 7890B-7000C, St. Clara, CA, USA) coupled with the Thermal Desorption (Markes, Unity-xr, London, UK) instrument. The reaction intermediate was monitored by Fourier transform spectroscopy (DRIFTS, Thermo Nicolet 6700, Waltham, MA, USA), and the experiment and instrument information are shown in Supplementary Material.

4. Conclusions

Manganese dioxides with different phases types (α , β , δ , and γ) were successfully composited with LaMnO₃ perovskite by a simple one-pot synthesis route. Combined with the characterization results of SEM, N₂ physisorption, XPS and H₂-TPR, the upgraded catalytic activity of the most active α -MnO₂/LaMnO₃ should be attributed to its high content of lattice oxygen, better low-temperature reducibility and larger surface area. The activation degree of lattice oxygen on the surface of MnO₂/LaMnO₃ can be controlled by adjusting the phase-type of MnO₂. In addition, the byproducts from the low-temperature oxidation of toluene over α -MnO₂/LaMnO₃ mainly include benzyl alcohol, benzaldehyde, benzoic acid, benzene, acetic acid, etc. This study also provides a method to control the crystal phase of manganese dioxide on the surface of perovskite and a demonstration to reveal the structure-activity relationship.

Supplementary Materials: The following supporting information can be downloaded at: <https://www.mdpi.com/article/10.3390/catal12121666/s1>, Figure S1: XRD patterns of LMO; Figure S2: Toluene oxidation over of (a) α -MO and α -MO/LMO, (b) β -MO and β -MO/LMO, (c) δ -MO and δ -MO/LMO, (d) γ -MO and γ -MO/LMO; Text S1: Chemicals and materials; Text S2: Characterization; Text S3: Preparation of LaMnO₃; Text S4: Preparation of MnO₂ with different crystal phases; Text S5: Normalized reaction rate equation [45–47].

Author Contributions: L.L. (Lu Li): Investigation, Data curation, Visualization, Writing—original draft, Funding acquisition; Y.L. and J.L.: Software, Supervision, writing—review & editing; B.Z.: Investigation, Validation, Methodology; M.G. and L.L. (Lizhong Liu): Resources, Funding acquisition, Project administration, Supervision, writing—review & editing. All authors have read and agreed to the published version of the manuscript.

Funding: This research was funded by the Natural Science Fundamental Research Project of Jiangsu Colleges and Universities of China (Grant No. 22KJB610022) and Jiangsu Provincial Key Research and Development Program (Grant No. BE2022767).

Data Availability Statement: Not applicable.

Acknowledgments: The authors of this work appreciate the technical support from the Instrumental Analysis Center of Xi'an Jiaotong University and Nantong University Analysis & Testing center.

Conflicts of Interest: The authors declare no conflict of interest.

References

1. Wang, X.; Sun, Y.; Li, M.; Zhang, W.; Zhu, Y. Excellent catalytic oxidation performance on toluene and benzene over OMS-2 with a hierarchical porous structure synthesized by a one-pot facile method: Modifying surface properties by introducing different amounts of K. *Catal. Sci. Technol.* **2022**, *12*, 2872–2886. [[CrossRef](#)]
2. Liu, B.; Ji, J.; Zhang, B.; Huang, W.; Gan, Y.; Leung, D.Y.C.; Huang, H. Catalytic ozonation of VOCs at low temperature: A comprehensive review. *J. Hazard. Mater.* **2022**, *422*, 126847. [[CrossRef](#)] [[PubMed](#)]
3. Li, S.; Wang, D.; Wu, X.; Chen, Y. Recent advance on VOCs oxidation over layered double hydroxides derived mixed metal oxides. *Chin. J. Catal.* **2020**, *41*, 550–560. [[CrossRef](#)]
4. Gao, Z.; Wang, J.; Muhammad, Y.; Hu, P.; Hu, Y.; Chu, Z.; Zhao, Z.; Zhao, Z. Hydrophobic shell structured NH₂-MIL(Ti)-125@mesoporous carbon composite via confined growth strategy for ultra-high selective adsorption of toluene under highly humid environment. *Chem. Eng. J.* **2022**, *432*, 134340. [[CrossRef](#)]
5. Guo, Y.; Wen, M.; Li, G.; An, T. Recent advances in VOC elimination by catalytic oxidation technology onto various nanoparticles catalysts: A critical review. *Appl. Catal. B Environ.* **2021**, *281*, 119447. [[CrossRef](#)]
6. Wu, P.; Jin, X.; Qiu, Y.; Ye, D. Recent progress of thermocatalytic and photo/thermocatalytic oxidation for VOCs purification over manganese-based oxide catalysts. *Environ. Sci. Technol.* **2021**, *55*, 4268–4286. [[CrossRef](#)]
7. Muir, B.; Sobczyk, M.; Bajda, T. Fundamental features of mesoporous functional materials influencing the efficiency of removal of VOCs from aqueous systems: A review. *Sci. Total Environ.* **2021**, *784*, 147121. [[CrossRef](#)]
8. Topuz, F.; Abdulhamid, M.A.; Hardian, R.; Holtzl, T.; Szekely, G. Nanofibrous membranes comprising intrinsically microporous polyimides with embedded metal–organic frameworks for capturing volatile organic compounds. *J. Hazard. Mater.* **2022**, *424*, 127347. [[CrossRef](#)]
9. Feng, Y.; Wang, C.; Wang, C.; Huang, H.; Hsi, H.-C.; Duan, E.; Liu, Y.; Guo, G.; Dai, H.; Deng, J. Catalytic stability enhancement for pollutant removal via balancing lattice oxygen mobility and VOCs adsorption. *J. Hazard. Mater.* **2022**, *424*, 127337. [[CrossRef](#)]
10. Li, J.; Zhang, M.; Elimian, E.A.; Lv, X.; Chen, J.; Jia, H. Convergent ambient sunlight-powered multifunctional catalysis for toluene abatement over in situ exsolution of Mn₃O₄ on perovskite parent. *Chem. Eng. J.* **2021**, *412*, 128560. [[CrossRef](#)]
11. Guo, M.; Liu, L.; Gu, J.; Zhang, H.; Min, X.; Liang, J.; Jia, J.; Li, K.; Sun, T. Catalytic performance improvement of volatile organic compounds oxidation over MnO_x and GdMnO₃ composite oxides from spent lithium-ion batteries: Effect of acid treatment. *Chin. J. Chem. Eng.* **2021**, *34*, 278–288. [[CrossRef](#)]
12. Liu, L.; Liu, R.; Xu, T.; Zhang, Q.; Tan, Y.; Zhang, Q.; Ding, J.; Tang, Y. Enhanced catalytic oxidation of chlorobenzene over MnO₂ grafted in situ by rare earth oxide: Surface doping induces lattice oxygen activation. *Inorg. Chem.* **2020**, *59*, 14407–14414. [[CrossRef](#)] [[PubMed](#)]
13. He, C.; Cheng, J.; Zhang, X.; Douthwaite, M.; Pattison, S.; Hao, Z. Recent advances in the catalytic oxidation of volatile organic compounds: A review based on pollutant sorts and sources. *Chem. Rev.* **2019**, *119*, 4471–4568. [[CrossRef](#)] [[PubMed](#)]
14. Royer, S.; Duprez, D.; Can, F.; Courtois, X.; Batiot-Dupeyrat, C.; Laassiri, S.; Alamdari, H. Perovskites as substitutes of noble metals for heterogeneous catalysis: Dream or reality. *Chem. Rev.* **2014**, *114*, 10292–10368. [[CrossRef](#)] [[PubMed](#)]
15. Zhu, J.; Li, H.; Zhong, L.; Xiao, P.; Xu, X.; Yang, X.; Zhao, Z.; Li, J. Perovskite oxides: Preparation, characterizations, and applications in heterogeneous catalysis. *ACS Catal.* **2014**, *4*, 2917–2940. [[CrossRef](#)]
16. Si, W.; Wang, Y.; Zhao, S.; Hu, F.; Li, J. A facile method for in situ preparation of the MnO₂/LaMnO₃ catalyst for the removal of toluene. *Environ. Sci. Technol.* **2016**, *50*, 4572–4578. [[CrossRef](#)]
17. Yang, J.; Li, L.; Yang, X.; Song, S.; Li, J.; Jing, F.; Chu, W. Enhanced catalytic performances of in situ-assembled LaMnO₃/δ-MnO₂ hetero-structures for toluene combustion. *Catal. Today* **2019**, *327*, 19–27. [[CrossRef](#)]
18. Liu, L.; Li, J.; Zhang, H.; Li, L.; Zhou, P.; Meng, X.; Guo, M.; Jia, J.; Sun, T. In situ fabrication of highly active γ-MnO₂/SmMnO₃ catalyst for deep catalytic oxidation of gaseous benzene, ethylbenzene, toluene, and o-xylene. *J. Hazard. Mater.* **2019**, *362*, 178–186. [[CrossRef](#)]
19. Figueredo, M.J.M.; Cocuzza, C.; Bensaid, S.; Fino, D.; Piumetti, M.; Russo, N. Catalytic abatement of volatile organic compounds and soot over manganese oxide catalysts. *Materials* **2021**, *14*, 4534. [[CrossRef](#)]
20. Kim, C.S.; Shim, G.W. Catalytic combustion of VOCs over a series of manganese oxide catalysts. *Appl. Catal. B Environ.* **2010**, *98*, 180–185. [[CrossRef](#)]

21. Liu, X.; Mi, J.; Shi, L.; Liu, H.; Liu, J.; Ding, Y.; Shi, J.; He, M.; Wang, Z.; Xiong, S.; et al. In situ modulation of a-site vacancies in LaMnO_{3.15} perovskite for surface lattice oxygen activation and boosted redox reactions. *Angew. Chem. Int. Edit.* **2021**, *60*, 26747–26754. [[CrossRef](#)] [[PubMed](#)]
22. Min, X.; Guo, M.; Li, K.; Gu, J.; Guo, X.; Xue, Y.; Liang, J.; Hu, S.; Jia, J.; Sun, T. Enhancement of toluene removal over α @ δ -MnO₂ composites prepared via one-pot by modifying the molar ratio of KMnO₄ to MnSO₄·H₂O. *Appl. Surf. Sci.* **2021**, *568*, 150972. [[CrossRef](#)]
23. Yang, W.; Su, Z.; Xu, Z.; Yang, W.; Peng, Y.; Li, J. Comparative study of α -, β -, γ - and δ -MnO₂ on toluene oxidation: Oxygen vacancies and reaction intermediates. *Appl. Catal. B Environ.* **2020**, *260*, 118150. [[CrossRef](#)]
24. Liu, L.; Liu, J.; Guo, M. One-pot synthesis of dual-phase manganese dioxide for toluene removal: Effect of crystal phase blending level on oxygen species and activity. *J. Environ. Chem. Eng.* **2022**, *10*, 107448. [[CrossRef](#)]
25. Li, K.; Chen, C.; Zhang, H.; Hu, X.; Sun, T.; Jia, J. Effects of phase structure of MnO₂ and morphology of δ -MnO₂ on toluene catalytic oxidation. *Appl. Surf. Sci.* **2019**, *496*, 143662. [[CrossRef](#)]
26. Huang, N.; Qu, Z.; Dong, C.; Qin, Y.; Duan, X. Superior performance of α @ β -MnO₂ for the toluene oxidation: Active interface and oxygen vacancy. *Appl. Catal. A-Gen.* **2018**, *560*, 195–205. [[CrossRef](#)]
27. Wang, D.; Wang, L.; Liang, G.; Li, H.; Liu, Z.; Tang, Z.; Liang, J.; Zhi, C. A superior δ -MnO₂ cathode and a self-healing Zn- δ -MnO₂ battery. *ACS Nano* **2019**, *13*, 10643–10652. [[CrossRef](#)]
28. Liu, L.; Zhang, H.; Jia, J.; Sun, T.; Sun, M. Direct molten polymerization synthesis of highly active samarium manganese perovskites with different morphologies for VOC removal. *Inorg. Chem.* **2018**, *57*, 8451–8457. [[CrossRef](#)]
29. Liu, L.; Zhou, B.; Liu, Y.; Liu, J.; Hu, L.; Tang, Y.; Wang, M. In-situ regulation of acid sites on Mn-based perovskite@mullite composite for promoting catalytic oxidation of chlorobenzene. *J. Colloid. Interf. Sci.* **2021**, *606*, 1866–1873. [[CrossRef](#)]
30. Ding, J.; Liu, L.; Xue, J.; Zhou, Z.; He, G.; Chen, H. Low-temperature preparation of magnetically separable Fe₃O₄@CuO-RGO core-shell heterojunctions for high-performance removal of organic dye under visible light. *J. Alloys Compd.* **2016**, *688*, 649–656. [[CrossRef](#)]
31. Liu, R.; Zhou, B.; Liu, L.; Zhang, Y.; Chen, Y.; Zhang, Q.; Yang, M.; Hu, L.; Wang, M.; Tang, Y. Enhanced catalytic oxidation of VOCs over porous Mn-based mullite synthesized by in-situ dismutation. *J. Colloid. Interf. Sci.* **2021**, *585*, 302–311. [[CrossRef](#)] [[PubMed](#)]
32. Si, W.; Wang, Y.; Peng, Y.; Li, J. Selective dissolution of A-site cations in ABO₃ perovskites: A new path to high-performance catalysts. *Angew. Chem. Int. Edit.* **2015**, *54*, 7954. [[CrossRef](#)] [[PubMed](#)]
33. Guo, M.; Wang, X.; Liu, L.; Min, X.; Hu, X.; Guo, W.; Zhu, N.; Jia, J.; Sun, T.; Li, K. Recovery of cathode materials from spent lithium-ion batteries and their application in preparing multi-metal oxides for the removal of oxygenated VOCs: Effect of synthetic methods. *Env. Res.* **2021**, *193*, 110563. [[CrossRef](#)] [[PubMed](#)]
34. Guo, M.; Li, K.; Zhang, H.; Min, X.; Liang, J.; Hu, X.; Guo, W.; Jia, J.; Sun, T. Promotional removal of oxygenated VOC over manganese-based multi oxides from spent lithium-ions manganate batteries: Modification with Fe, Bi and Ce dopants. *Sci. Total Environ.* **2020**, *740*, 139951. [[CrossRef](#)]
35. Chen, J.; Chen, X.; Yan, D.; Jiang, M.; Xu, W.; Yu, H.; Jia, H. A facile strategy of enhancing interaction between cerium and manganese oxides for catalytic removal of gaseous organic contaminants. *Appl. Catal. B Environ.* **2019**, *250*, 396–407. [[CrossRef](#)]
36. Li, X.; Zhu, Z.; Zhao, Q.; Wang, L. Photocatalytic degradation of gaseous toluene over ZnAl₂O₄ prepared by different methods: A comparative study. *J. Hazard. Mater.* **2011**, *186*, 2089–2096. [[CrossRef](#)]
37. Chen, J.; Chen, X.; Xu, W.; Xu, Z.; Chen, J.; Jia, H.; Chen, J. Hydrolysis driving redox reaction to synthesize Mn-Fe binary oxides as highly active catalysts for the removal of toluene. *Chem. Eng. J.* **2017**, *330*, 281–293. [[CrossRef](#)]
38. Gao, J.; Tong, X.; Li, X.; Miao, H.; Xu, J. The efficient liquid-phase oxidation of aromatic hydrocarbons by molecular oxygen in the presence of MnCO₃. *J. Chem. Technol. Biot.* **2007**, *82*, 620–625. [[CrossRef](#)]
39. Pan, H.; Jian, Y.; Chen, C.; He, C.; Hao, Z.; Shen, Z.; Liu, H. Sphere-shaped Mn₃O₄ catalyst with remarkable low-temperature activity for methyl-ethyl-ketone combustion. *Environ. Sci. Technol.* **2017**, *51*, 6288–6297. [[CrossRef](#)]
40. Gennequin, C.; Kouassi, S.; Tidahy, L.; Cousin, R.; Lamonier, J.F.; Garcon, G.; Shirali, P.; Cazier, F.; Aboukais, A.; Siffert, S. Co-Mg-Al oxides issued of hydrotalcite precursors for total oxidation of volatile organic compounds. Identification and toxicological impact of the by-products. *Comptes Rendus Chim.* **2010**, *13*, 494–501. [[CrossRef](#)]
41. Deng, J.; Zhang, L.; Dai, H.; He, H.; Au, C.T. Strontium-doped lanthanum cobaltite and manganite: Highly active catalysts for toluene complete oxidation. *Ind. Eng. Chem. Res.* **2008**, *47*, 8175–8183. [[CrossRef](#)]
42. Liu, Y.; Dai, H.; Deng, J.; Du, Y.; Li, X.; Zhao, Z.; Wang, Y.; Gao, B.; Yang, H.; Guo, G. In situ poly(methyl methacrylate)-templating generation and excellent catalytic performance of MnO_x/3DOMLaMnO₃ for the combustion of toluene and methanol. *Appl. Catal. B Environ.* **2013**, *140*, 493–505. [[CrossRef](#)]
43. Liu, L.; Sun, J.; Ding, J.; Zhang, Y.; Sun, T.; Jia, J. Highly active Mn_{3-x}Fe_xO₄ spinel with defects for toluene mineralization: Insights into regulation of the oxygen vacancy and active metals. *Inorg. Chem.* **2019**, *58*, 13241–13249. [[CrossRef](#)] [[PubMed](#)]
44. Liu, L.; Sun, J.; Ding, J.; Zhang, Y.; Jia, J.; Sun, T. Catalytic oxidation of VOCs over SmMnO₃ perovskites: Catalyst synthesis, change mechanism of active species, and degradation path of toluene. *Inorg. Chem.* **2019**, *58*, 14275–14283. [[CrossRef](#)] [[PubMed](#)]
45. Zhao, J.; Xi, W.; Tu, C.; Dai, Q.; Wang, X. Catalytic oxidation of chlorinated VOCs over Ru/Ti_xSn_{1-x} catalysts. *Appl. Catal. B* **2020**, *263*, 118237. [[CrossRef](#)]

-
46. Schmid, D.; Micic, V.; Laumann, S.; Hofmann, T. Measuring the reactivity of commercially available zero-valent iron nanoparticles used for environmental remediation with iopromide. *J. Contam. Hydrol.* **2015**, *181*, 36–45. [[CrossRef](#)]
 47. Yang, P.; Fan, S.; Chen, Z.; Bao, G.; Zuo, S.; Qi, C. Synthesis of Nb₂O₅ based solid superacid materials for catalytic combustion of chlorinated VOCs. *Appl. Catal. B* **2018**, *239*, 114–124. [[CrossRef](#)]